The Canadian Mineralogist
Vol. 57, pp. 663-675 (2019)
DOI: 10.3749/canmin.1900035

SYNTHESIS AND STABILITY OF SOME MEMBERS OF THE PHARMACOSIDERITE GROUP, $A Fe_4(OH)_4(AsO_4)_3 \cdot nH_2O$ (A = K, Na, 0.5Ba, 0.5Sr)

JURAJ MAJZLAN[§] AND PATRICK HAASE

Institutes of Geosciences, Friedrich-Schiller University, Burgweg 11, D-07749 Jena, Germany

JAKUB PLÁŠIL

Institute of Physics ASCR, v.v.i., Na Slovance 1999/2, 18221 Praha 8, Czech Republic

EDGAR DACHS

Department of Chemistry and Physics of Materials, Division Mineralogy, University of Salzburg, Jakob-Haringerstrasse 2A, A-5020 Salzburg, Austria

ABSTRACT

Samples of the pharmacosiderite group were synthesized either directly, from aqueous solutions at 160 °C, or by ion exchange over extended periods of time at 100 °C. In more than 200 experiments, no pure pharmacosiderite sample was obtained, and a protocol was developed to remove scorodite and arsenical iron oxides from the samples. In this way, K-, Na-, Ba-, and Sr-dominant pharmacosiderite samples were prepared. The chemical compositions of the two samples used for further experiments were $Ba_{0.702}Fe_4[(AsO_4)_{0.953}(SO_4)_{0.047}]_3(OH)_{3.455}O_{0.545} \cdot 5.647H_2O$ and $K_{1.086}Fe_4[(AsO_4)_{0.953}(SO_4)_{0.047}]_3(OH)_{3.772}O_{0.228} \cdot 4.432H_2O$. The Ba-dominant pharmacosiderite is tetragonal at room temperature, and the K-dominant pharmacosiderite is cubic. Upon heating, both samples lose zeolitic H_2O (shown by thermogravimetry), and this loss is accompanied by unit-cell contraction. In Ba-dominant pharmacosiderite, this loss also seems to be responsible for a symmetry change from tetragonal to cubic. The slight unit-cell contraction in Ba-dominant pharmacosiderite at <100 °C might be attributed to either negative thermal expansion or minor H_2O loss; our data cannot differentiate between these two possibilities. Both samples persisted in a crystalline state up to 320 °C (the highest temperature of the powder XRD experiment), showing that pharmacosiderite is able to tolerate almost complete removal of the zeolitic H_2O molecules. Low-temperature heat capacity measurements show a diffuse magnetic anomaly for K-dominant pharmacosiderite at ≈5 K and a sharp lambda transition for Ba-dominant pharmacosiderite at 15.2 K. The calculated standard entropy at $T = 298.15$ is 816.9 ± 5.7 J/molK for K-dominant pharmacosiderite (molecular mass 824.2076 g/mol, see formula above) and 814.1 ± 5.5 J/molK for Ba-dominant pharmacosiderite (899.7194 g/mol).

Keywords: pharmacosiderite, thermodynamics, crystal structure, *in situ* heating.

INTRODUCTION

The first description of pharmacosiderite can probably be attributed to Klaproth (1786, p. 161) who described "dark green cubes, with flat and lustrous faces, on a grey copper ore in quartz" from Cornwall, England. He noted that the mineral could easily be confused with fluorite, but the chemical analysis gave copper and arsenic, and "it seemed that there is some iron". Interestingly, this earliest analysis was based on his visual (color of the product after reduction on charcoal and melting with borax) and olfactory (smell of arsenic fumes) perceptions. This ferric arsenate mineral was named pharmacosiderite by Hausmann (1813), who referred to five other contributions that listed the mineral under the names *Würfelerz* (cube ore) or *fer arseniaté*. He included the chemical analyses of Chenevix (1801) to support the

[§] *Corresponding author*: e-mail Juraj.Majzlan@uni-jena.de; telephone +49-3641-948700; fax +49-3641-948602

mineral's definition. Both of these sources concluded that the mineral is a ferric arsenate; Chenevix (1801, p. 221) found 9 wt.% copper oxide in his sample, but he commented that this ore was "mixed accidentally with a little copper". Leonhard (1821) listed other synonyms, such as *hexaedrisches Lirokon-Malachit*, but did not provide any new analytical data.

The principal features of the crystal structure of pharmacosiderite were established by Hägele & Machatschki (1937), Zemann (1948), and Buerger *et al*. (1967). Up to today, more than 50 structures closely related to pharmacosiderite have been refined. They are discussed in detail by Baur (2012) and comprise not only arsenates but also silicates, phosphates, and germanates. Their symmetries are cubic ($P\bar{4}3m$, $I\bar{4}3m$, $I23$), tetragonal ($P\bar{4}2m$, $P\bar{4}b2$), or trigonal ($R3m$) (Hager *et al*. 2010, Baur 2012). The cubic symmetry, indicated by the morphology of the crystals, is often not compatible with the optical anisotropy (Hartley 1900, Heide 1928), but this conflict has long been ignored (*cf*., Baur 2012, p. 17). The structure of pharmacosiderite is a rigid, but open, heteropolyhedral framework, with exchangeable cations and H_2O molecules in the large tunnels. The structural details of this group of phases are beyond the scope of this paper and can be found in Baur (2012).

The chemical compositions of the arsenate pharmacosiderite phases, as well as an understanding of their crystal structures, is also not a simple matter. The nominal formulae for pharmacosiderite and bariopharmacosiderite are $KFe_4(OH)_4(AsO_4)_3{\cdot}nH_2O$ and $Ba_{0.5}Fe_4(OH)_4(AsO_4)_3{\cdot}nH_2O$, respectively. The more trivial problem is the variable water content, not surprising for a zeolite-like phase. However, a number of studies reported a significant excess of exchangeable cations, such as K, Na, or Ba, in pharmacosiderite. Hager *et al*. (2010) reviewed the available, but sparse, data for natural pharmacosiderite samples (Walenta 1966, Peacor & Dunn 1985, Mutter *et al*. 1984) and showed that bariopharmacosiderite may contain up to 1.0 Ba atom per formula unit (*pfu*). The possibility of charge balance *via* reduction of Fe^{3+} to Fe^{2+} was excluded by Mössbauer spectroscopy (Mutter *et al*. 1984). Another, more viable, possibility is the removal of H^+ ions from the structure, either by deprotonation of a H_2O molecule (Walenta 1966) or dehydroxylation of a bridging OH group (Hager *et al*. 2010). The latter possibility seems to be more likely, although it is not conclusively proven. If so, the formula $Ba_{0.5}Fe_4(OH)_4(AsO_4)_3{\cdot}nH_2O$ changes to $BaFe_4(OH)_3O(AsO_4)_3{\cdot}nH_2O$ for 1 Ba *pfu*, and in the extreme case of dehydroxylation to $Ba_{2.5}Fe_4O_4(AsO_4)_3{\cdot}nH_2O$ for the maximal number of Ba *pfu*. The general formula that describes this substitution is then $Ba_{0.5+x}Fe_4(AsO_4)_3(OH)_{4-2x}O_{2x}{\cdot}nH_2O$. A similar set of formulae can be derived for the K-endmember pharmacosiderite, or other compositions that are either endmembers or intermediate compositions. The compositional variations are further complicated by the substitution of both monovalent and divalent ions (Na, K, Ba) on the exchangeable site, plus substitution on the tetrahedral site (As, P, S).

Despite the assertion of Hager *et al*. (2010) that pharmacosiderite-group minerals are rare, they occur at many sites, but usually in small amounts (Handbook of Mineralogy: Anthony *et al*. 2019). Detailed studies of localities with secondary ferric arsenates (*e.g*., Sejkora *et al*. 2006) show that pharmacosiderite occurs at these studied sites as a minor, often inconspicuous, phase. At some localities, pharmacosiderite may be an important or the dominant carrier of arsenic (Morin *et al*. 2002, Morin & Calas 2006, Bossy *et al*. 2010, Drahota *et al*. 2009, 2018, Herrmann *et al*. 2018). Such occurrences seem to be linked to slow weathering under circumneutral conditions. Hence, even at sites where substantial acidity is developed, pharmacosiderite could crystallize in microenvironments that are able to neutralize that acidity. New and recently described minerals of this group include hydroniumpharmacosiderite (Mills *et al*. 2010a), cesiumpharmacosiderite (Mills *et al*. 2013), thalliumpharmacosiderite (Rumsey *et al*. 2014), and plumbopharmacosiderite (Vignola *et al*. 2018).

In this work, we have developed a synthesis protocol for arsenate pharmacosiderite without the use of organic, organometallic, or complex compounds that are commonly used for the syntheses of the titanosilicate (*e.g*., Chapman & Roe 1990, Gerasimova *et al*. 2013, Xu *et al*. 2000, 2004) and germanate (*e.g*., Nenoff *et al*. 1994) pharmacosiderites. The synthesis of arsenate pharmacosiderite has been described by Wada & Okada (1976), Hager *et al*. (2011), and Okuma *et al*. (2018). It is possible to exchange the mono- and divalent cations in the synthesized samples and to create pharmacosiderite phases of different compositions. The pharmacosiderite crystals were subjected to powder X-ray diffraction (pXRD); single-crystal diffraction measurements were done, but the data were difficult to interpret. Thermal stability was tested in heating experiments up to 320 °C, coupled with *in situ* pXRD. Using several well-characterized and pure samples, heat capacities and standard entropies were measured by relaxation calorimetry.

For clarity, hereafter we use a different terminology in this paper than that which is standard for the minerals of this group. The mineral name "pharmacosiderite" is usually reserved for compositions near $KFe_4(OH)_4(AsO_4)_3{\cdot}5H_2O$. In this work, we refer to

this composition as K-dominant pharmacosiderite in order to explicitly distinguish this phase from Na-dominant pharmacosiderite (natropharmacosiderite), Ba-dominant pharmacosiderite (bariopharmacosiderite), or Sr-dominant pharmacosiderite (strontiopharmacosiderite).

Methods

The powder X-ray diffraction (pXRD) analyses were conducted with a Bruker D8 Advance diffractometer in the angular range 5–90° 2θ at room temperature with Cu*K*α radiation. The step size was set to 0.01° 2θ and the dwell time to 1 s per step. In order to reduce the noise of the Fe fluorescence excited by Cu emission radiation from the iron-rich samples, the energy window of the Lynxeye detector was set to 0.18–0.25 V.

Variable-temperature pXRD data were collected with the same instrument, equipped with a temperature stage (CHC+ Plus cryo and humidity chamber, Anton-Paar GmbH, Graz, Austria) fitted with a platinum heater. A Pt 100 temperature sensor was integrated in the sample holder for accurate measurement and control of the temperature. The *in situ* diffraction data were either collected in air from 20 to 300 °C or in vacuum from 20 to 400 °C, in both cases with a temperature step of 20 °C. The XRD patterns were measured from 5° to 60° 2θ, with a step of 0.02° 2θ and counting time of 2.5 s per step. All data sets were processed with a full-profile refinement using the program GSAS (Larson & von Dreele 1994).

Crystalline products of the syntheses were also checked by single-crystal X-ray diffraction in order to verify the correct symmetry and refine the crystal structure of both pharmacosiderite-related synthetic phases. These studies were done with a single-crystal X-ray Rigaku SuperNova diffractometer equipped with an Atlas S2 detector, employing the mirror-monochromatized Mo*K*α radiation (λ = 0.71073 Å) from a micro-focus X-ray tube, providing a high-flux brilliant beam. For structure refinements, the Jana2006 program was used (Petříček *et al*. 2014).

The images of selected carbon-coated samples were acquired with a field-emission gun scanning electron microscope (SEM) Zeiss Ultra Plus with an accelerating voltage of 2 kV. Semiquantitative energy-dispersive (EDX) analyses were obtained with the same instrument, using an acceleration voltage of 20 kV.

Thermogravimetric (TG) and differential thermal (DT) studies were done with a TG 92 Setaram TG/DTA instrument. The samples were heated from room temperature to 900 °C in a flow of argon at a heating rate of 10 °C/min.

Total digestion with a mixture of HNO_3, $HClO_4$, and HF was used to dissolve a portion of each sample. The elemental composition of the aqueous samples was determined by inductively coupled plasma (ICP) optical emission spectrometry (ICP-OES) using a Variant 725 ICP-OES equipped with a charge-coupled device (CCD) detector.

Small portions of the synthetic samples were embedded in epoxy and prepared in the form of polished sections. After carbon coating, they were examined in an electron microprobe JEOL JXA-8230 (Jena) to obtain back-scattered electron (BSE) images, energy-dispersive (EDX) analyses, and wavelength-dispersive (WDX) analyses. The samples were found to be extremely sensitive to both the vacuum inside the instrument and the electron beam. Numerous desiccation cracks made it difficult to find suitable spots for analysis. Where found, the analytical results were strongly dependent on the sample current; for example, a change of current from 15 to 5 nA resulted in a change of the reported Fe_2O_3 concentration by 4 wt.%. Hence, even the reported WDX analyses (Table S1[1]) are considered only as semiquantitative and are used to support the bulk chemical analyses of our samples.

The heat capacity of the pharmacosiderite samples between 2 and 300 K was measured by relaxation calorimetry using a commercial Physical Properties Measurement System (PPMS, from Quantum Design, San Diego, California, USA) at the University of Salzburg, Austria. With due care, accuracy can be within 1% from 5 to 300 K, and within 5% for 0.7 to 5 K (Kennedy *et al*. 2007). Powdered samples were wrapped in a thin Al foil and compressed to produce a ≈0.5 mm thick pellet, which was then placed onto the sample platform of the calorimeter for measurement.

Materials

For all syntheses, mixtures of deionized water, $FeCl_2{\cdot}4H_2O$, $FeCl_3{\cdot}6H_2O$, $Fe(NO_3)_3{\cdot}9H_2O$, $FeSO_4{\cdot}4H_2O$, $Fe_2(SO_4)_3{\cdot}nH_2O$, K_2SO_4, KNO_3, KCl, K_2CO_3, $NaNO_3$, $Na_2H(AsO_4){\cdot}7H_2O$, and As_2O_5 were used. The chemicals were of analytical grade and were used as purchased, without any purification. None of the >200 experiments with variable initial

[1] Supplementary Data are available from the Depository of Unpublished data on the MAC website (http://mineralogicalassociation.ca/), document "pharmacosiderite group synthesis, CM57, 19-00035".

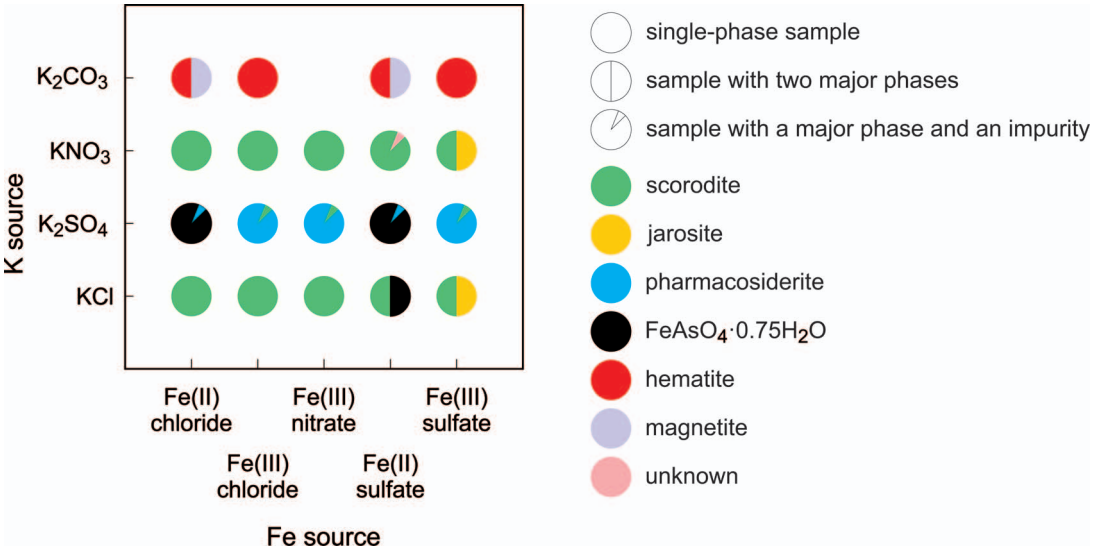

FIG. 1. Graphical summary of the syntheses carried out in this work. Solutions of the chemicals shown in this figure were mixed and treated hydrothermally at 160 °C. The source of arsenic was $Na_2H(AsO_4)\cdot 7H_2O$ and As_2O_5 (the latter usually giving better results). For additional details, see the MATERIALS section.

concentrations, reaction time, and temperature yielded pure pharmacosiderite. Many experiments produced scorodite, $FeAsO_4\cdot 0.75H_2O$, arsenolite, dussertite, jarosite, goethite, hematite, magnetite, an amorphous product, or a mixture thereof (Fig. 1). We also attempted to decompose natural arsenopyrite to produce pharmacosiderite; these syntheses failed, as the initial product showed little sign of decomposition at different pH values after 14 days at 200 °C in water.

Only ferric iron compounds as the source of iron led to the precipitation of pharmacosiderite (Fig. 1). For arsenic, both $Na_2H(AsO_4)\cdot 7H_2O$ and As_2O_5 were used, the latter giving slightly better results.

Synthesis of samples with K- and Na-dominant pharmacosiderite

To synthesize K-dominant pharmacosiderite, 1.0 g $FeCl_3\cdot 6H_2O$ (Alfa Aesar, 97%) and 0.4252 g As_2O_5 (Alfa Aesar, 99.9%) were dissolved in 5 mL and 10 mL deionized H_2O, respectively, in separate beakers ($n_{Fe} = n_{As} = 3.7$ mmol). Both solutions were poured into a Teflon container (internal volume of 100 mL) which was then placed in a steel autoclave. A solution of K_2SO_4 was prepared by dissolving K_2SO_4 in hot water at 80 °C until saturation was reached. Afterwards, each of the beakers (from the dissolution of $FeCl_3\cdot 6H_2O$ and As_2O_5) was rinsed with still hot 10 mL saturated K_2SO_4 solution (Bernd Kraft, >99%), and the solutions were quickly transferred into the same Teflon container. Then, an additional 10 mL of the hot saturated K_2SO_4 solution was added to the suspension. The result is a total volume of 45 mL, of which 30 mL is saturated K_2SO_4 solution. After mixing the solutions, the liquid turned into a milky-yellow-greenish suspension. The steel autoclave was sealed and kept at 160 °C for three days. After removal from the oven and cooling, the product was filtered and washed with deionized H_2O.

Experiments with variable synthesis temperatures (Fig. 2a) showed that the product is completely X-ray amorphous at 110 and 120 °C. At temperatures above 140 °C, the product is dominated by pharmacosiderite, but the scorodite impurity is always present. Experiments with variable synthesis times (Fig. 2b) at 160 °C showed that at least two days were necessary for a product dominated by pharmacosiderite. There were some variations in the abundance of pharmacosiderite and scorodite beyond the two days. It is not clear if the two phases actually transform back and forth to each other, or if the syntheses are so sensitive to the starting conditions that these experiments yield somewhat erratic results.

The synthesis of Na-dominant pharmacosiderite was carried out with 1.0 g $FeCl_3\cdot 6H_2O$ (Alfa Aesar, 97%) and 0.4252 g As_2O_5 (Alfa Aesar, 99.9%), dissolved separately in 5 and 10 mL of deionized H_2O. Saturated Na_2SO_4 solution (GPR Rectapur, 100%; saturated at 40 °C) was adjusted to pH 6.5 with diluted H_2SO_4 and NaOH. Mixing of the solutions proceeded as in the case of the K-dominant

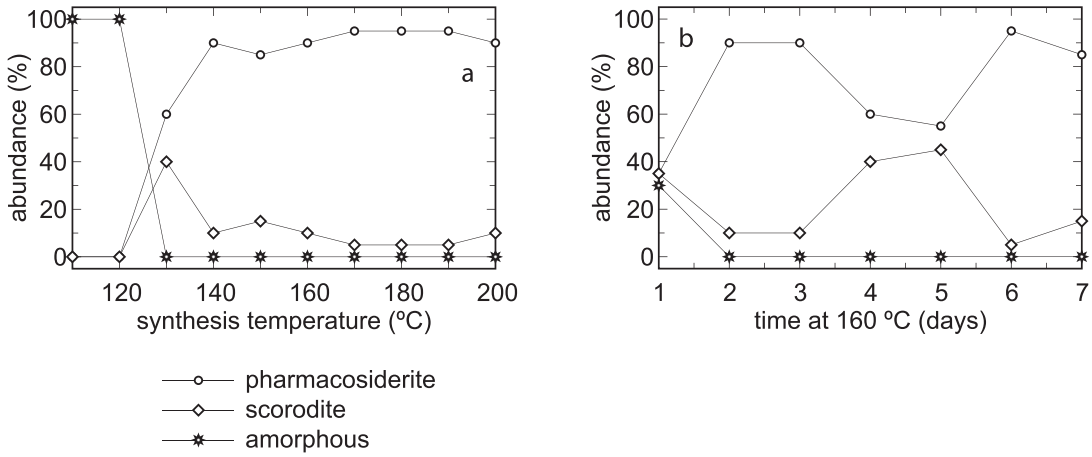

FIG. 2. (a) Abundance of pharmacosiderite, scorodite, and X-ray amorphous material in syntheses at variable temperatures. (b) Abundance of the three phases in syntheses at 160 °C with variable times.

pharmacosiderite synthesis (see above). The final suspension was sealed in a Teflon container (internal volume of 100 mL) which was placed in a steel autoclave and kept at 160 °C for seven days.

Removal of impurities

Powder XRD analysis of the samples extracted from the Teflon containers indicated that the products are mixtures of pharmacosiderite (green, strong vitreous luster, transparent, cubic crystals) and scorodite (pale grey-green, radial aggregates) (Fig. 3a, b). SEM images (Fig. 3a, b) further showed the presence of an Fe oxide, which was probably X-ray amorphous.

The whole uncrushed precipitate was washed with 30 mL 1 M KOH (Merck, ≥84%, pellets) for 60 min with continuous stirring at ambient temperature to decompose the scorodite. During this step, arsenic was leached from the scorodite and the X-ray amorphous Fe oxide (Harvey *et al*. 2006, Tanno *et al*. 2011). Scorodite was replaced by X-ray amorphous arsenian Fe oxides that maintained the shape of the original aggregates (Fig. 3c, d). After this treatment, the color of the sample changed from green to brown (Heide 1928, Buerger *et al*. 1967). The product was filtered and washed with deionized H_2O.

After the KOH treatment, an acidic solution (30 mL deionized H_2O and 12 drops of 10% HCl) was used to dissolve the X-ray amorphous iron oxides. The KOH-treated sample was mixed with the weak acid, and the suspension was left being continuously stirred at ambient temperature for two days. The suspension was filtered after this and the solid sample was re-suspended in a fresh weak acid for another two days. The color of the pharmacosiderite changed from brown to green within the first minutes (Mills *et al*. 2010b) due to the treatment with an acidic solution (Heide 1928, Buerger *et al*. 1967). After the treatment with the acidic solution, the product was filtered and washed again with deionized H_2O. Inspection of secondary electron images (Fig. 3e) showed only imprints of the scorodite aggregates in the pharmacosiderite cubes, and scorodite and iron oxides were no longer seen in the samples (Fig. 3f).

Cation exchange

The K-dominant pharmacosiderite sample used in further experiments (see below) was treated with 100 mL of 0.5 M KCl (Bernd Kraft) at 100 °C for two weeks. This treatment was done in order to remove H_3O^+ cations which could have been incorporated during the acidic wash of the sample.

The K-dominant pharmacosiderite sample without KCl treatment was used for cation exchange. Separate batches of such K-dominant pharmacosiderite were treated with 100 mL of 0.5 M $SrCl_2{\cdot}6H_2O$ or 100 mL of 0.3 M $Ba(NO_3)_2$ (Alfa Aesar, 99%) and kept in closed borosilicate bottles at 100 °C for two weeks to exchange the ions within the tunnels of the structure to obtain Sr- and Ba-dominant-pharmacosiderite.

Synthesis of hydronium-dominant pharmacosiderite was attempted but was not successful. The monomineralic K-dominant pharmacosiderite (whose synthesis was described above) was either treated with 100 mL deionized H_2O and 40 drops of 10% HCl, or with 100 mL deionized H_2O and 40 drops of 9.8% H_2SO_4 (as in Mills *et al*. 2010b). Both batches were kept separately in closed borosilicate bottles at 100 °C for two weeks to exchange the ions within the tunnels

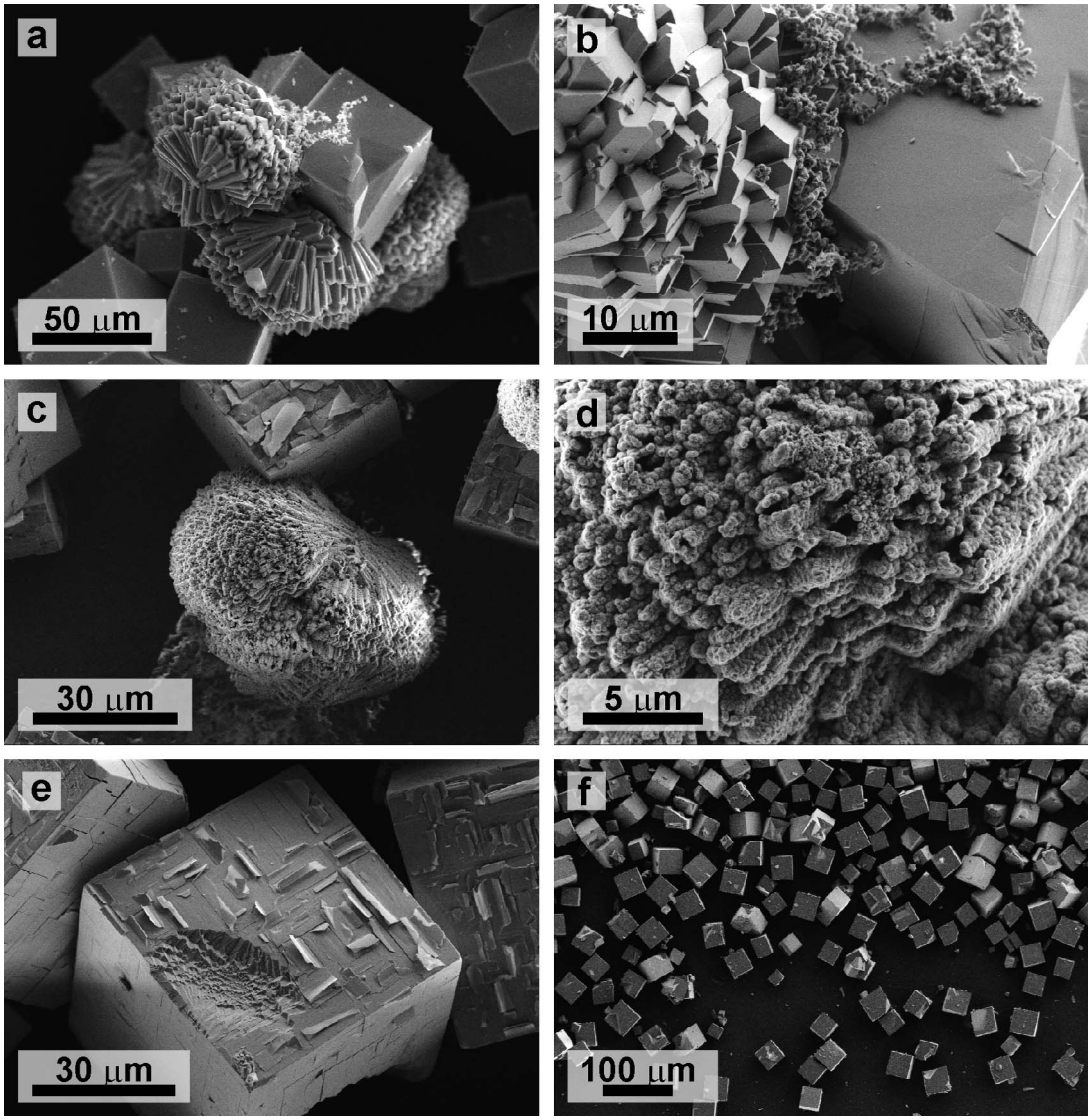

FIG. 3. Back-scattered electron (BSE) and secondary electron (SE) images of the synthesis products at different stages of the syntheses. (a, b) Cubic pharmacosiderite crystals intergrown with rosettes of scorodite crystals. (b) Fine-grained X-ray amorphous oxides are visible coating the surface of the pharmacosiderite crystals. (c, d) The synthesis product after washing with the alkaline KOH solution. Scorodite transforms to pseudomorphs of arsenian iron oxides [in the center in (c), detail in (d)]. (e) The synthesis product after washing with the acidic HCl solution, showing pharmacosiderite crystals with imprints of the dissolved pseudomorphs of arsenian iron oxides after scorodite. (f) The final product composed of cubic crystals and penetration twins of pharmacosiderite.

of the structure to obtain fully exchanged hydroniumpharmacosiderite. SEM images showed that the cubic crystals crumble and fall apart. The EDX analysis indicated the presence of potassium within the subhedral grains, confirming that the exchange was far from complete.

RESULTS AND DISCUSSION

The samples with pharmacosiderite as the only phase consisted of euhedral cubic crystals or penetration twins of pharmacosiderite with sizes up to 50 μm (Fig. 3f). Treatment with alkaline and acidic solutions

TABLE 1. CHEMICAL COMPOSITION OF THE PHARMACOSIDERITE SAMPLES

	As_2O_5	BaO	Fe_2O_3	K_2O	Na_2O	SO_3	SrO	H_2O	Total
Ba-ph	36.81	11.84	35.15	0.00	0.19	1.26	0.00	14.77	100
K-ph	40.29	0.01	38.16	6.11	0.22	1.39	0.00	13.81	100
	As	Ba	Fe	K	Na	S	Sr	As+S	
Ba-ph	2.910	0.702	4.000	0.000	0.055	0.143	0.000	3.053	
K-ph	2.935	0.000	4.000	1.086	0.060	0.146	0.000	3.081	

H_2O content measured by thermogravimetry; the other oxides calculated from the ICP analytical results. The upper block of the table gives wt.% of oxides. The lower block gives the atomic proportions in a formula normalized to Fe = 4.000.

caused some peeling of the surface layers (Fig. 3e), but these flakes retained the pharmacosiderite structure, as no other phase was detected by pXRD.

Chemical composition

The chemical composition of the pharmacosiderite samples was established by wet-chemical analyses using ICP methods. The results, re-calculated to 100 wt.%, including water content (determined from thermogravimetry, see below), are listed in Table 1. The bulk analyses are supported by the results from the electron microprobe (EMP) (Table S1) which are considered to be only semiquantitative for the reasons listed above.

The chemical analyses confirmed complete cation exchange for Ba- and Sr-dominant pharmacosiderite. All of the samples were contaminated with small amounts of sulfur and a minor Na impurity. Substitution of arsenate for sulfate is not hampered by spatial requirements (S^{6+} is smaller than As^{5+}), but by the heterovalent nature of that substitution. The sum of the tetrahedral cations ($S^{6+} + As^{5+}$) is slightly greater than the expected 3 (it varies between 3.0 and 3.1). The samples show substantial cation excess on the exchangeable site (mono- and divalent cations).

An excess of exchangeable cations is known (*cf.*, INTRODUCTION) and is most likely compensated by dehydroxylation of the pharmacosiderite structure. For Ba-dominant pharmacosiderite, the general formula is $Ba_{0.5+x}Fe_4(AsO_4)_3(OH)_{4-2x}O_{2x}\cdot nH_2O$. Including the As–S substitution, the general formula becomes $Ba_{0.5+x}Fe_4[(AsO_4)_y(SO_4)_{1-y}]_3(OH)_{4-2x-3(1-y)}O_{2x+3(1-y)}\cdot nH_2O$. For the composition of our sample, the formula was $Ba_{0.702}Fe_4[(AsO_4)_{0.953}(SO_4)_{0.047}]_3(OH)_{3.455}O_{0.545}\cdot 5.647H_2O$.

Similarly, for K-dominant pharmacosiderite, the general formula is $K_{1+x}Fe_4[(AsO_4)_y(SO_4)_{1-y}]_3(OH)_{4-x-3(1-y)}O_{x+3(1-y)}\cdot nH_2O$. For the composition of our sample the formula was $K_{1.086}Fe_4[(AsO_4)_{0.953}(SO_4)_{0.047}]_3(OH)_{3.772}O_{0.228}\cdot 4.432H_2O$.

Crystal structure

Single-crystal X-ray diffraction experiments only partially confirmed the results of previous studies. In general, the structural architecture is the same as that reported in previous studies, although the current results suggest that there may be differences in the details. The unit-cell parameters of the synthetic Ba-dominant pharmacosiderite conform to tetragonal symmetry [a = 7.9791(3) Å, c = 8.0817(5) Å, V = 514.53(4) Å^3] (*e.g.*, Grey *et al*. 2014). The crystals are twinned by merohedry and adopt a $P\bar{4}2m$ space group, but the structural refinement was unstable and led to some unrealistic twin fractions. Nevertheless, the tetragonal symmetry is in line with the fact that the analyzed synthetic Ba-dominant pharmacosiderite has an elevated H_2O content, as was also confirmed in the current study (thermogravimetry).

Single-crystal X-ray diffraction experiments on the synthetic K-dominant pharmacosiderite showed that the crystals are cubic [$a_{subcell}$ = 8.0120(4) Å]. Careful examination of diffraction frames revealed additional reflections, halving **a***, which do not originate from reticular twinning, but most probably correspond to a superstructure lattice. The reason for this is probably due to the ordering of K and OH within the structure. A detailed study of these phenomena lies beyond the scope of the current paper and will be the subject of future research.

High-temperature behavior – thermogravimetry

Heating to 900 °C (Fig. 4) showed H_2O loss in two stages. The first stage centered at ≈200 °C is the loss of molecular H_2O and it ceased at around 250–280 °C. The second stage is centered at ≈460 °C, generating weaker TG and DT signals, and corresponds to the dehydroxylation of the structure. At ≈550 °C, the masses of the samples stabilize and are constant up to ≈850 °C, when both As and S can vaporize and escape from the sample.

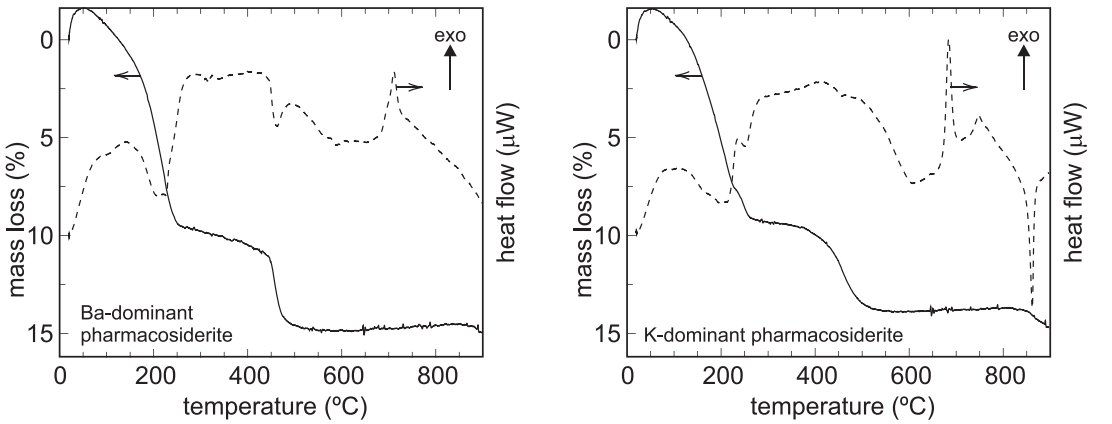

FIG. 4. Thermogravimetric (solid curves) and differential thermal (dashed curves) data for synthetic K- and Ba-dominant pharmacosiderite.

There were additional transformations seen in the temperature range between 600 and 800 °C. They were not accompanied by mass variations, only by strong DTA signals.

High-temperature behavior – in situ pXRD

The K- and Ba-dominant pharmacosiderite samples were selected for these experiments. The results are graphically summarized in Figures 5 and 6.

The Ba-dominant pharmacosiderite sample was tetragonal at room temperature. Upon heating, the unit-cell volume decreased slightly up to 80 °C (Table 2). The thermogravimetry curve in this region is dominated by buoyancy effects, and it cannot be established if the sample loses H_2O. The unit-cell volume decrease could be due to such a minor H_2O loss, or it could be attributed to negative thermal expansion. Negative thermal expansion is known, especially for corner-connected polyhedral networks (*e.g.*, Tao & Sleight 2003), and the pharmacosiderite framework belongs to this group of compounds. Its structure is closely related to that of ReO_3 (Baur 2012), and ReO_3 is well-known as a material with negative thermal expansion (*e.g.*, Chatterji *et al*. 2008).

There is a slight expansion of the unit cell up to 120 °C, followed by a dramatic contraction (Fig. 5a). The contraction can easily be correlated to the major H_2O loss. In this process, starting at ≈170 °C, the tetragonal splitting of the XRD peaks is lifted and the peak intensity diminishes significantly (Fig. 5b). Despite these changes, the pXRD pattern could still be indexed with a cubic pharmacosiderite cell. The cubic cell expands up to 300 °C, while the intensities of the XRD peaks remain more or less constant. At 320 °C, the final measurement temperature, the pharmacosiderite framework undergoes another collapse. After cooling to room temperature, the pXRD pattern shows a cubic cell, with intensities similar to those observed at 320 °C.

A very similar thermal behavior was also reported for a trigonal titanosilicate pharmacosiderite by Ferdov (2012). This compound showed a slight decrease in unit-cell volume upon heating to 75 °C, followed by two large contractions of the unit-cell volume at 100 and 150 °C. At 125 °C, the symmetry of the structure changed from trigonal ($R3m$) to cubic ($P\bar{4}3m$), thus appearing analogous to what we observed in our experiments.

Hager *et al*. (2010) described two polymorphs of Ba-rich pharmacosiderite, one cubic and one tetragonal. They differed by the distribution of the Ba^{2+} cations in the unit cell, but also by their H_2O content. The H_2O-poorer phase had cubic symmetry, while the H_2O-richer phase had tetragonal symmetry. Hence, one may speculate that these two phases are not polymorphs, but their symmetry is a function of H_2O content, in addition to the differences in the positions of the Ba^{2+} ions as described by Hager *et al*. (2010). If so, the phase transformation observed here could be induced either by temperature or by solid solution formation (or both) (*cf*. Heaney 2000). Such an idea is further supported by studies of cubic and trigonal germanate pharmacosiderite phases (Nenoff *et al*. 1994), whose symmetry can be reversibly controlled by cation and anion exchange.

The K-dominant pharmacosiderite sample was cubic at room temperature, and the symmetry did not change during heating (Fig. 6). The unit-cell volume decreased slightly up to 100 °C (Table 3), and then it dropped significantly as a response to H_2O loss from the structure. The unit cell contracted by 2.8% at 180

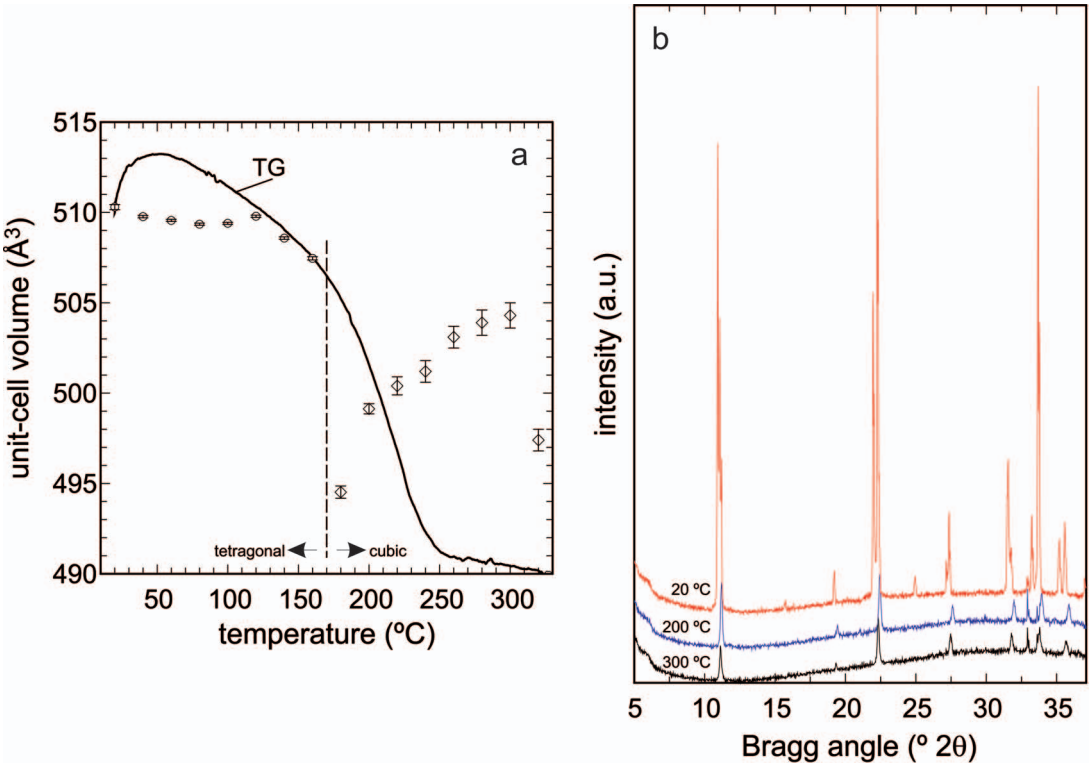

FIG. 5. (a) Changes in the unit-cell volume of Ba-dominant pharmacosiderite as a function of temperature. The symmetry of the sample changes from tetragonal to cubic during heating, as indicated in the figure. The thick curve (marked TG) is the thermogravimetric trace, shown for easier correlation with the observed variations of the unit-cell volume. (b) Powder XRD patterns of the Ba-dominant pharmacosiderite sample at selected temperatures. Note the decrease in the intensity but retention of crystallinity up to 300 °C and the lifting of the tetragonal splitting of the peaks during heating.

TABLE 2. LATTICE PARAMETERS OF Ba-DOMINANT PHARMACOSIDERITE AS A FUNCTION OF TEMPERATURE

Temperature (°C)	*a* (Å)	*c* (Å)
20	7.9586(11)	8.0566(17)
40	7.9609(6)	8.0436(7)
60	7.9615(5)	8.0391(6)
80	7.9594(4)	8.0399(6)
100	7.9586(5)	8.0423(6)
120	7.9591(5)	8.0475(6)
140	7.9588(6)	8.0290(7)
160	7.9494(6)	8.0303(12)
180	7.9079(31)	
200	7.9324(25)	
220	7.939(4)	
240	7.944(5)	
260	7.954(6)	
280	7.958(6)	
300	7.960(7)	
320	7.923(5)	

TABLE 3. LATTICE PARAMETERS OF K-DOMINANT PHARMACOSIDERITE AS A FUNCTION OF TEMPERATURE

Temperature (°C)	*a* (Å)
40	7.99864(20)
60	8.00084(19)
80	7.99641(21)
100	7.9958(6)
120	7.98565(25)
140	7.9633(4)
160	7.9483(7)
180	7.92260(28)
200	7.92588(29)
220	7.9296(4)
240	7.9316(4)
260	7.9406(11)
280	7.9376(5)
300	7.9376(6)

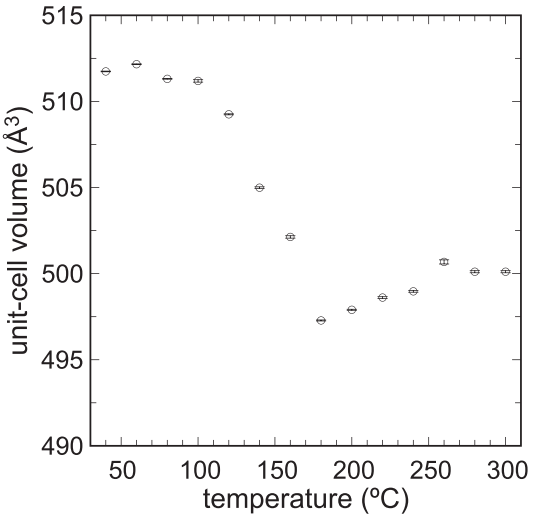

FIG. 6. Changes in the unit-cell volume of K-dominant pharmacosiderite as a function of temperature.

°C compared to its size at room temperature. Afterwards, the unit-cell volume increased continuously up to 300 °C, the highest temperature of our experiment. At 300 °C, the intensity of the XRD peaks decreased by 80% from their values at room temperature, but the patterns could still be easily indexed with the cubic cell and the lattice parameters extracted with acceptable precision. Hence, our results show that the structure is capable of tolerating near-complete loss of zeolitic H_2O without collapse of the tunnels.

Low-temperature behavior – relaxation calorimetry

The results of the low-temperature heat capacity measurements are shown graphically in Figure 7a, with the numerical results given in Tables S2 and S3. The smoothed thermodynamic functions for both samples are presented in Tables S4 and S6. Functions used for the fitting are specified in Table S5 and S7. In addition to the two samples prepared in this study, another data set for the composition $(H_3O)Fe_4(AsO_4)_3(OH)_4{\cdot}5.5H_2O$ (Okuma *et al.* 2018) was included. These data were kindly provided to us by R. Okuma. All samples show anomalous C_p behavior at low temperatures, related to the magnetic contribution to C_p. For K-dominant pharmacosiderite, there is only a weak hump centered at $T \approx 5$ K, similar to that seen in the H_3O-rich pharmacosiderite (Fig. 7b). On the other hand, Ba-dominant pharmacosiderite shows a pronounced lambda-shaped anomaly at $T = 15.1$ K. Perhaps the differences in the magnetic behavior at

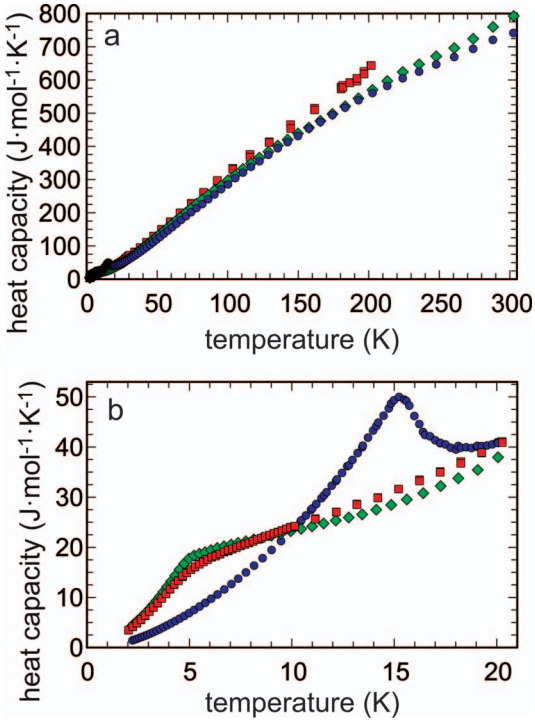

FIG. 7. (a) Low-temperature heat capacity and (b) magnetic anomalies in the low-temperature heat capacity of K- (green diamonds), Ba- (blue circles), and H_3O- (red squares) dominant pharmacosiderite. Data for H_3O-rich pharmacosiderite from Okuma *et al.* (2018).

low temperatures are related to the puzzling structural properties of the pharmacosiderite samples.

No other C_p anomalies are visible in the data, thus confirming the absence of Fe-arsenate or Fe-sulfate impurities. These experiments confirm that the scorodite impurity was completely removed by the alkaline-acid treatment.

The C_p data were used for the calculation of standard entropies for K- and Ba-dominant pharmacosiderite. The data for H_3O-rich pharmacosiderite were only measured up to 200 K and cannot be used for calculation of the standard entropy. The entropies were calculated for the formulae listed above. For K-dominant pharmacosiderite (molecular mass 824.2076 g/mol), the entropy at $T = 298.15$ is 816.9 ± 5.7 J/molK. For Ba-dominant pharmacosiderite (molecular mass 899.7194 g/mol), the entropy at $T = 298.15$ is 814.1 ± 5.5 J/molK. The entropy of H_3O-rich pharmacosiderite, although not calculated, appears to be higher than those of K- and Ba-dominant pharmacosiderite, probably because of the significant entropic contribution of the H_3O^+ group.

Thermodynamic properties

Solution calorimetry was attempted on the samples in this work. Pharmacosiderite has proven to be unusually stable in contact with acids and showed no signs of dissolution in 5 N HCl, our usual calorimetric solvent, even after a day. The samples did dissolve rapidly in molten sodium molybdate (high-temperature oxide melt) at $T = 700$ °C. The heat effects were very large, leading to large uncertainties. In addition, the processed results indicated that pharmacosiderite is remarkably insoluble in water, as much as three orders of magnitude less soluble [for As(V)] than scorodite. Such information requires further validation because high-temperature oxide-melt calorimetry of heavily hydrated phases can be plagued with systematic errors. Hence, we have refrained from giving numerical values for the enthalpies of dissolution and formation, as these could be used by an uncritical reader to generate thermodynamic models that are incorrect. The recent work of Das (2019) provided some thermodynamic data relevant to pharmacosiderite-like clusters using *ab initio* methods. Their direct use in low-temperature geochemistry is limited.

Conclusions

This work presents a protocol for the synthesis of pure pharmacosiderite samples. Although the synthesis of this phase has been the subject of several patents (Wada & Okada 1976, Hager *et al*. 2011), it is not clear to what extent their samples, intended for industrial use, were free of impurities. Investigation of the behavior of pharmacosiderite at high temperatures suggested several possible new directions of research, for example the prospect of negative thermal expansion. A novel, although unfinished, part of this work is the determination of the thermodynamic functions of pharmacosiderite. We will attempt to make progress on this in the near future.

Acknowledgments

We appreciate the reviewers' constructive comments. This work was supported financially by a *Deutsche Forschungsgemeinschaft* grant MA 3927/23-1. We wish to thank R. Okuma for the primary C_p data for hydroniumpharmacosiderite. Help with the electron microprobe and thermogravimetry by S. Kiefer and B. Kreher-Hartmann was greatly appreciated.

References

Anthony, J.W., Bideaux, R.A., Bladh, K.W., & Nichols, M.C., Eds. (2019) Handbook of Mineralogy. Mineralogical Society of America, Chantilly, Virginia 20151-1110, USA. http://www.handbookofmineralogy.org/pdfs/pharmacosiderite.pdf. [date accessed: December 30, 2018]

Baur, W.H. (2012) Rigid frameworks of zeolite-like compounds of the pharmacosiderite structure-type. *Microporous and Mesoporous Materials* **151**, 13–25.

Bossy, A., Grosbois, C., Beauchemin, S., Courtin-Nomade, A., Hendershot, W., & Bril, H. (2010) Alteration of As-bearing phases in a small watershed located on a high grade arsenic-geochemical anomaly (French Massif Central). *Applied Geochemistry* **25**, 1889–1901.

Buerger, M.J., Dollase, W.A., & Garaycochea-Wittke, I. (1967) The structure and composition of the mineral pharmacosiderite. *Zeitschrift für Kristallographie* **125**, 92–108.

Chapman, D.M. & Roe, A.L. (1990) Synthesis, characterization and crystal chemistry of microporous titanium-silicate materials. *Zeolites* **10**, 730–737.

Chatterji, T., Henry, P.F., Mittal, R., & Chaplot, S.L. (2008) Negative thermal expansion of ReO_3: Neutron diffraction experiments and dynamical lattice calculations. *Physical Review B* **78**, 134105.

Chenevix, R. (1801) Analysis of the arseniates of copper, and of iron, described in the preceding paper; likewise an analysis of the red octahedral copper ore of Cornwall; with remarks on some particular modes of analysis. *Philosophical Transactions of the Royal Society of London* **91**, 193–240.

Das, B. (2019) Theoretical study of formation of secondary arsenic minerals: Scorodite and pharmacosiderite. *ACS Earth Space Chemistry* **3**, 192–201.

Drahota, P., Rohovec, J., Filippi, M., Mihaljevič, M., Rychlovsky, P., Červeny, V., & Pertold, Z. (2009) Mineralogical and geochemical controls on arsenic speciation and mobility under different redox conditions in soil, sediment and water at the Mokrsko-West gold deposit, Czech Republic. *Science of Total Environment* **407**, 3372–3384.

Drahota, P., Kulakowski, O., Culka, A., Knappová, M., Rohovec, J., Veselovský, F., & Racek, M. (2018) Arsenic mineralogy of near-neutral soils and mining waste at the Smolotely-Líšnice historical gold district, Czech Republic. *Applied Geochemistry* **89**, 243–254.

Ferdov, S. (2012) Thermal flexibility of microporous titanosilicate with distorted pharmacosiderite structure. *Microporous and Mesoporous Materials* **159**, 96–99.

Gerasimova, L.G., Maslova, M.V., & Nikolaev, A.I. (2013) Synthesis of the new nano-porous titanosilicates using ammonium oxysulphotitanite. *Glass Physics and Chemistry* **39**, 602–608.

Grey, I.E., Mumme, W.G., Price, J.R., Mills, S.J., Macrae, C.M., & Favreau, G. (2014) Ba–Cu ordering in bariopharmacoalumite-*Q2a2b2c* from Cap Garonne, France. *Mineralogical Magazine* **78**, 851–860.

HÄGELE, G. & MACHATSCHKI, F. (1937) Synthese des Alumopharmakosiderits; Formel und Struktur des Pharmakosiderits. *Fortschritte der Mineralogie* **21**, 77–78.

HAGER, S.L., LEVERETT, P., WILLIAMS, P.A., MILLS, S.J., HIBBS, D.E., RAUDSEPP, M., KAMPF, A.R., & BIRCH, W.D. (2010) The single-crystal X-ray structures of bariopharmacosiderite-C, bariopharmacosiderite-Q and natropharmacosiderite. *Canadian Mineralogist* **48**, 1477–1485.

HAGER, S., LEVERETT, P., & WILLIAMS, P. (2011) Synthesis of pharmacosiderite minerals. Australian Patent AU2011901933. Filing date 2011-05-18, Publication date 2011-06-02.

HARTLEY, E.G.J. (1900) Ueber die Zusammensetzung der natürlichen Arsenate und Phosphate. *Zeitschrift für Kristallographie* **32**, 220–226.

HARVEY, M.C., SCHREIBER, M.E., RIMSTIDT, J.D., & GRIFFITH, M.M. (2006) Scorodite dissolution kinetics: Implications for arsenic release. *Environmental Science & Technology* **40**, 6709–6714.

HAUSMANN, J.F.L. (1813) *Handbuch der Mineralogie*. Vandenhoeck & Ruprecht, Göttingen, Germany, 1065–1067.

HEANEY, P.J. (2000) Phase transformations induced by solid solution. *Reviews in Mineralogy and Geochemistry* **39**, 135–174.

HEIDE, F. (1928) Über eine hydrothermale Paragenesis von Quarz und Arsenmineralien im veränderten Quarzporphyr vom Saubach i. V. und über einige Eigenschaften des Pharmakosiderits und des Symplesits. *Zeitschrift für Kristallographie* **67**, 33–90.

HERRMANN, J., VOEGELIN, A., PALATINUS, L., MANGOLD, S., & MAJZLAN, J. (2018) Secondary Fe-As-Tl mineralization in soils near Buus in the Swiss Jura Mountains. *European Journal of Mineralogy* **30**, 887–898.

KENNEDY, C.A., STANCESCU, M., MARRIOTT, R.A., & WHITE, M.A. (2007) Recommendations for accurate heat capacity measurements using a Quantum Design physical property measurement system. *Cryogenics* **47**, 107–112.

KLAPROTH, M.H. (1786) Mineralogisch-chemischer Beytrag zur Naturgeschichte Cornwallischer Mineralien. *Schriften der Gesellschaft naturforschender Freunde in Berlin* **7**, 141–196.

LARSON, A.C. & VON DREELE, R.B. (1994) *GSAS*: General Structure Analysis System. LANSCE, MS-H805, Los Alamos, New Mexico.

LEONHARD, K.C. (1821) *Handbuch der Oryktognosie: für akademische Vorlesungen und zum Selbststudium*. Mohr und Winter, Heidelberg, Germany, 363.

MILLS, S.J., KAMPF, A.R., WILLIAMS, P.A., LEVERETT, P., POIRIER, G., RAUDSEPP, M., & FRANCIS, C.A. (2010a) Hydroniumpharmacosiderite, a new member of the pharmacosiderite supergroup from Cornwall, UK: structure and description. *Mineralogical Magazine* **74**, 863–869.

MILLS, S.J., HAGER, S.L., LEVERETT, P., WILLIAMS, P.A., & RAUDSEPP, M. (2010b) The structure of H_3O^+-exchanged pharmacosiderite. *Mineralogical Magazine* **74**, 487–492.

MILLS, S.J., PETRINI, E., BELLATRECCIA, F., SCHLÜTER, J., KAMPF, A.R., RUMSEY, M.S., DINI, M., & SPRATT, J. (2013) Caesiumpharmacosiderite, IMA 2013-096. *CNMNC Newsletter* **18**, 3257; *Mineralogical Magazine* **77**, 3249–3258.

MORIN, G. & CALAS, G. (2006) Arsenic in soils, mine tailings, and former industrial sites. *Elements* **2**, 97–101.

MORIN, G., LECOCQ, D., JUILLOT, F., CALAS, G., ILDEFONSE, P., BELINE, S., BRIOIS, V., DILLMANN, P., CHEVALLIER, C., GAUTHIER, C., SOLE, A., PETIT, P.-E., & BORENSZTAJN, S. (2002) EXAFS evidence of sorbed arsenic(V) and pharmacosiderite in a soil overlying the Echassieres geochemical anomaly, Allier, France. *Bulletin de la Societe Geologique de France* **173**, 281–291.

MUTTER, G., EYSEL, W., GREIS, O., & SCHMETZER, K. (1984) Crystal chemistry of natural and ion-exchanged pharmacosiderites. *Neues Jahrbuch für Mineralogie Monatshefte*, 183–192.

NENOFF, T.M., HARRISON, W.T.A., & STUCKY, G.D. (1994) $Na_3H_x(H_2PO_4)_x[(GeO)_4(GeO_4)_3]\cdot 4H_2O$: A rhombohedrally-distorted germanium pharmacosiderite analog with anion/cation exchange capabilities. *Chemistry of Materials* **6**, 525–530.

OKUMA, R., YAJIMA, T., FUJII, T., TAKANO, M., & HIROI, Z. (2018) Frustrated magnetism of pharmacosiderite comprising tetrahedral clusters arranged in the primitive cubic lattice. *Journal of the Physical Society of Japan* **87**, 093702.

PEACOR, D.R. & DUNN, P.J. (1985) Sodium-pharmacosiderite, a new analog of pharmacosiderite from Australia and new occurrences of barium-pharmacosiderite. *Mineralogical Record* **16**, 121–124.

PETŘÍČEK, V., DUŠEK, M., & PALATINUS, L. (2014) Crystallographic computing system JANA2006: general features. *Zeitschrift für Kristallographie* **229**, 345–352.

RUMSEY, M.S., MILLS, S.J., SPRATT, J., HAY, D.G., & FARBER, G. (2014) Thalliumpharmacosiderite, IMA 2013-124. *CNMNC Newsletter* **20**, 553; *Mineralogical Magazine* **78**, 549–558.

SEJKORA, J., ONDRUŠ, P., FIKAR, M., VESELOVSKÝ, F., MACH, Z., GABAŠOVÁ, A., ŠKODA, R., & BERAN, P. (2006) Supergene minerals at the Huber stock and Schnöd stock deposits, Krásno ore district, the Slavkovský les area, Czech Republic. *Journal of Czech Geological Society* **51**, 57–101.

TANNO, T., FUJIEDSA, S., SHINODA, K., & SUZUKI, S. (2011) Synthesis of large porous particles of iron oxide and their

arsenic characteristics in aqueous solution. *High Temperature Materials and Processes* **30**, 305–310.

Tao, J.Z. & Sleight, A.W. (2003) The role of rigid unit modes in negative thermal expansion. *Journal of Solid State Chemistry* **173**, 442–448.

Vignola, P., Rotiroti, N., Hatert, F., Dal Bo, F., Gentile, P., Albertini, C., Merlini, M., Risplendente, A., & Pavese, A. (2018) Plumbopharmacosiderite, $Pb_{0.5}Fe_4^{3+}(AsO_4)_3(OH)_4{\cdot}5H_2O$, a new mineral species from the Monte Falo Pb-Zn mine near the village of Coiromonte in the Armeno municipality, Novara province, Italy. *Canadian Mineralogist* **56**, 143–150.

Wada, T. & Okada, K. (1976) Method for the production of a zeolite material. United States Patent 3,981,970. Filing date July 16, 1971, Issue date September 21, 1976.

Walenta, K. (1966) Beiträge zur Kenntnis seltener Arsenatminerale unter besonderer Berücksichtigung von Vorkommen des Schwarzwalds. *Tschermaks Mineralogische und Petrographische Mitteilungen* **11**, 121–164.

Xu, H., Navrotsky, A., Nyman, M.D., & Nenoff, T.M. (2000) Thermochemistry of microporous silicotitanate phases in the Na_2O–Cs_2O–SiO_2–TiO_2–H_2O system. *Journal of Materials Research* **15**, 815–823.

Xu, H., Navrotsky, A., Nyman, M.D., & Nenoff, T.M. (2004) Crystal chemistry and energetics of pharmacosiderite-related microporous phases in the K_2O–Cs_2O–SiO_2–TiO_2–H_2O system. *Microporous and Mesoporous Materials* **72**, 209–218.

Zemann, J. (1948) Formel und Strukturtyp des Pharmakosiderits. *Tschermaks Mineralogische und Petrographische Mitteilungen* **1**, 1–13.

Received April 29, 2019. Revised manuscript accepted June 27, 2019.